



Co₃O₄ nanoparticles decorated Ag₃PO₄ tetrapods as an efficient visible-light-driven heterojunction photocatalyst



Chunni Tang^{a,b}, Enzhou Liu^a, Jun Wan^a, Xiaoyun Hu^c, Jun Fan^{a,*}

^a School of Chemical Engineering, Northwest University, Xi'an 710069, PR China

^b Department of Chemical Engineering, Shaanxi Institute of Technology, Xi'an 710300, PR China

^c School of Physics, Northwest University, Xi'an 710069, PR China

ARTICLE INFO

Article history:

Received 20 June 2015

Received in revised form 21 August 2015

Accepted 29 August 2015

Available online 1 September 2015

Keywords:

Cobalt oxide
Silver phosphate
Heterojunction
Photocatalysis

ABSTRACT

Novel Ag₃PO₄ tetrapods with exposed {1 1 1} facets were synthesized via a facile precipitation method, and then Co₃O₄ nanoparticles were decorated on the surface of Ag₃PO₄ tetrapods using an impregnation method. On top of the superior photocatalytic performance of highly reactive {1 1 1} facets of Ag₃PO₄ tetrapods, the Co₃O₄/Ag₃PO₄ heterostructured photocatalyst exhibited further improved efficiency in photodegrading methyl blue (MB) under visible light irradiation (>400 nm). In addition, the Co₃O₄ content and calcination temperature had significant impacts on the photocatalytic activities of the samples. The highest efficiency was observed on the 2.0 wt% Co₃O₄/Ag₃PO₄ heterojunction calcined at 673 K. The improved photocatalytic performance could be mainly attributed to accelerated electron-hole separation by p–n junctions in Co₃O₄/Ag₃PO₄ heterojunction, and the enhanced structural stabilities may be due to the protection of insoluble Co₃O₄ and the effect of Ag⁰ on the surface of Ag₃PO₄. Moreover, h⁺ played the major role in the MB decolorization.

© 2015 Elsevier B.V. All rights reserved.

1. Introduction

Semiconductor photocatalysis has attracted considerable attention attributing to the fact that it provides a new way to meet the challenges of environmental pollution and energy crises [1,2]. Unfortunately, most widely employed semiconductor photocatalysts are only active under UV-light irradiation, but photocatalysis using visible light could be highly economical compared to the process using an artificial UV-light source. Therefore, development of efficient visible light driven photocatalysts is a major challenge in this field. Recently, silver orthophosphate (Ag₃PO₄) has been reported as a promising photocatalytic material due to its very high photocatalytic activity under visible light irradiation [3]. This novel photocatalyst can achieve a quantum efficiency of up to 90% at wavelengths greater than 420 nm, which is significantly higher than the previous reported values. However, Ag₃PO₄ photocatalyst is still facing the same challenges encountered by most photocatalysts, such as the fast recombination of photo-generated charge carriers. Moreover, Ag₃PO₄ also suffers from stability issue in practical applications because it is photosensitive and slightly soluble in aqueous solution. Thus, diverse techniques have been proposed to

improve its activity and stability, i.e. morphology control, surface modification and element doping [4–13]. Very recently, coupling Ag₃PO₄ with other materials is regarded as a good strategy to design efficient and stable photocatalysts, such as, coupling with inorganic materials (TiO₂, SnO₂, ZnO, CeO₂, Fe₂O₃, AgX (X = Cl, Br, I), Bi₂WO₆, BiPO₄, BiOI, WO₃, Ag₂O, etc.) and organic materials (MoS₂, C₃N₄, graphene oxide, graphene, carbon nanotubes and carbon quantum dots, etc.) [14–29].

Co₃O₄ is a p-type semiconductor with the characteristics of high thermal and chemical stability, low solubility, interesting electronic, magnetic and catalytic properties [30], as well as narrow band gap (about 1.2–2.1 eV) [31,32]. Due to its excellent properties, Co₃O₄ can be applied as a photocatalyst or co-catalyst for the visible-light-driven photocatalytic reactions [33–35]. For example, Co₃O₄/BiOCl photocatalyst exhibited an enhanced photocatalytic activity under visible light in the decomposition of Rhodamine B (RhB) and methylenorange (MO) compared with pure BiOCl [36]. Because Ag₃PO₄ is suggested to be a n-type semiconductor as indicated by the positive photocurrent at anodic potential [3], and the valence band (VB) of Ag₃PO₄ (about 2.67 eV vs NHE) [37] is positive than that of Co₃O₄ (about 2.44 eV vs NHE) [31]. Therefore, the combination of Co₃O₄ and Ag₃PO₄ can easily form a p–n heterojunction and the photogenerated holes on the VB of the Ag₃PO₄ can be easily transferred to Co₃O₄, promoting the effective separation of photo-generated electrons and holes of Ag₃PO₄. Moreover, because of the

* Corresponding author. Fax: +86 29 88302223.
E-mail address: fanjun@nwnu.edu.cn (J. Fan).

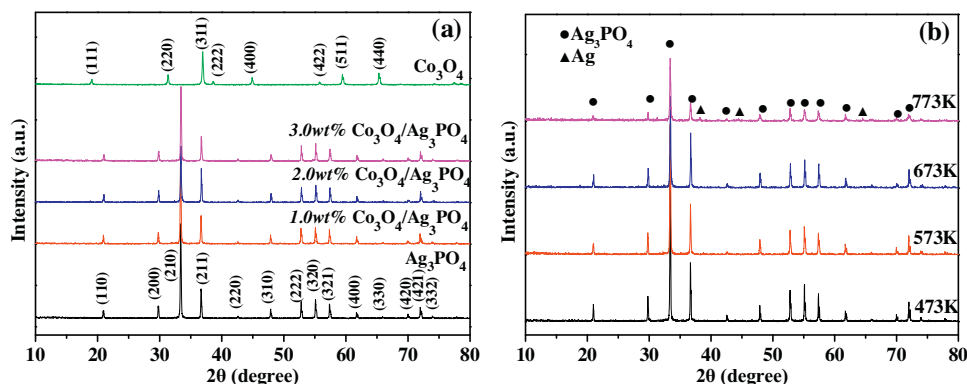


Fig. 1. XRD patterns of the samples: (a) Co_3O_4 , Ag_3PO_4 and $\text{Co}_3\text{O}_4/\text{Ag}_3\text{PO}_4$ composites with different Co_3O_4 content calcined at 673 K, (b) the 2.0 wt% $\text{Co}_3\text{O}_4/\text{Ag}_3\text{PO}_4$ composites calcined at different temperature.

chemical stability and low solubility of Co_3O_4 , loading Co_3O_4 on the surface of Ag_3PO_4 could effectively protect the Ag_3PO_4 from dissolution in aqueous solutions and enhance its stability during the photocatalytic process.

Evidenced by theoretical and experimental research, the {111} facets of Ag_3PO_4 are much more reactive than {110} and {100}. Zheng et al. [38] found the dispersion between the valence bands and conduction bands of the {111} surface was beneficial for the separation of photogenerated electrons and holes on the {111} surface, which improved the photocatalytic activity of the {111} surface. Martin et al. [39] attributed the excellent and reproducible performance of {111} terminated tetrahedrons of Ag_3PO_4 to a synergistic effect between high surface energy and a small hole mass, leading to high charge carrier mobility and active surface reaction sites. Given this, a cooperative effect of active facets and heterojunction may enhance the photocatalytic activity and stability of Ag_3PO_4 together.

In this paper, novel Ag_3PO_4 tetrapods with exposed {111} facets were synthesized by a facile precipitation method and then Co_3O_4 nanoparticles were decorated on the surface of Ag_3PO_4 tetrapods using an impregnation method. The photocatalytic performances were evaluated by photodegradation of methyl blue (MB) under the visible light irradiation. The effects of Co_3O_4 content and calcination temperature on photocatalytic activity were also investigated. In addition, the photodegradation mechanism on $\text{Co}_3\text{O}_4/\text{Ag}_3\text{PO}_4$ was also discussed.

2. Experimental

2.1. Preparation of Ag_3PO_4

The tetrapod-shaped Ag_3PO_4 microcrystals were prepared through a facile precipitation process. Typically, AgNO_3 (0.2 g) was dissolved in distilled water, and concentrated ammonia aqueous solution ($\text{NH}_3\text{H}_2\text{O}$, mass fraction 25–28%) was added to form a transparent solution. Then the above $[\text{Ag}(\text{NH}_3)_2]^+$ complex was directly poured into the aqueous solution containing the PEG (0.3 M) and Na_2HPO_4 (0.5 M) at 333 K. After stirring for 1 h, the products were collected by centrifugation, washed for several times and dried at 333 K overnight. For comparison, irregular Ag_3PO_4 crystals were synthesized by direct precipitation method as follows: Na_2HPO_4 solution was added drop by drop to the AgNO_3 solution under stirring. After stirring for 1 h, the above suspension experienced centrifugation, washing and drying.

2.2 Preparation of $\text{Co}_3\text{O}_4/\text{Ag}_3\text{PO}_4$ composites

The $\text{Co}_3\text{O}_4/\text{Ag}_3\text{PO}_4$ composites were prepared via a facile impregnation method. In a typical procedure, the as-prepared Ag_3PO_4 tetrapods were added into distilled water containing an

appropriate amount of $\text{Co}(\text{NO}_3)_2$. The suspension was sonicated for 0.5 h to completely disperse the Ag_3PO_4 crystals, followed by stirring until the water was volatilized completely at 333 K. The resulting powder was collected and calcinated at different temperature for 2 h in the air. The collected product was denoted as x wt% $\text{Co}_3\text{O}_4/\text{Ag}_3\text{PO}_4$, and the weight percentages of Co_3O_4 in the initial photocatalyst precursors were from 0 to 3.0 wt%. Co_3O_4 was prepared by calcining the $\text{Co}(\text{NO}_3)_2$ at 673 K for 2 h in the air.

2.2. Characterization

The X-ray diffraction (XRD) of the products was examined on a Rigaku-Dmax 3C diffractometer using $\text{Cu K}\alpha$ radiation ($\lambda = 1.54 \text{ \AA}$). The morphology of samples were observed by a JSM-6390A scanning electron microscope (SEM) and equipped with energy-dispersive X-ray (EDS). The surface area measurement was carried out by the N_2 adsorption isotherms conducted in the Quantachrome NOVA 2000e using the Brunauer-Emmette-Teller (BET) method. Fourier transform infrared (FT-IR) spectra were collected on PerkinElmer Frontier. Besides, UV–vis absorption spectra were recorded using a Shimadzu UV-3600 UV/Vis/NIR spectrophotometer with BaSO_4 as a reference. X-ray photoelectron spectroscopy (XPS) data were collected from a Kratos AXIS NOVA spectrometer, and PL spectra were measured at room temperature on a Hitachi F-7000 fluorescence spectrophotometer.

2.3. Photocatalytic tests

The photocatalytic activities of samples were examined with visible light ($\lambda > 400 \text{ nm}$)-induced photodegradation of MB in an aqueous solution. In a typical photodegradation process, 40 mg photocatalysts were added into 50 mL MB solution (10 mg/L). Prior to irradiation, the suspensions were magnetically stirred in dark for 0.5 h to ensure the adsorption-desorption equilibrium of MB on the surface of photocatalysts. A 300 W Xe lamp (Beijing Perfect-light Technology Co. Ltd., China, Microsolar 300UV) with a 400 nm cut off filter was used as visible light source, which was positioned on the top of the reaction cell. The above suspension was stirred with bubbling of air throughout the tests at room temperature. The decolorization of MB was determined by measuring the absorbance of the solution at 664 nm using a Shimadzu UV-3600 UV/Vis/NIR spectrophotometer.

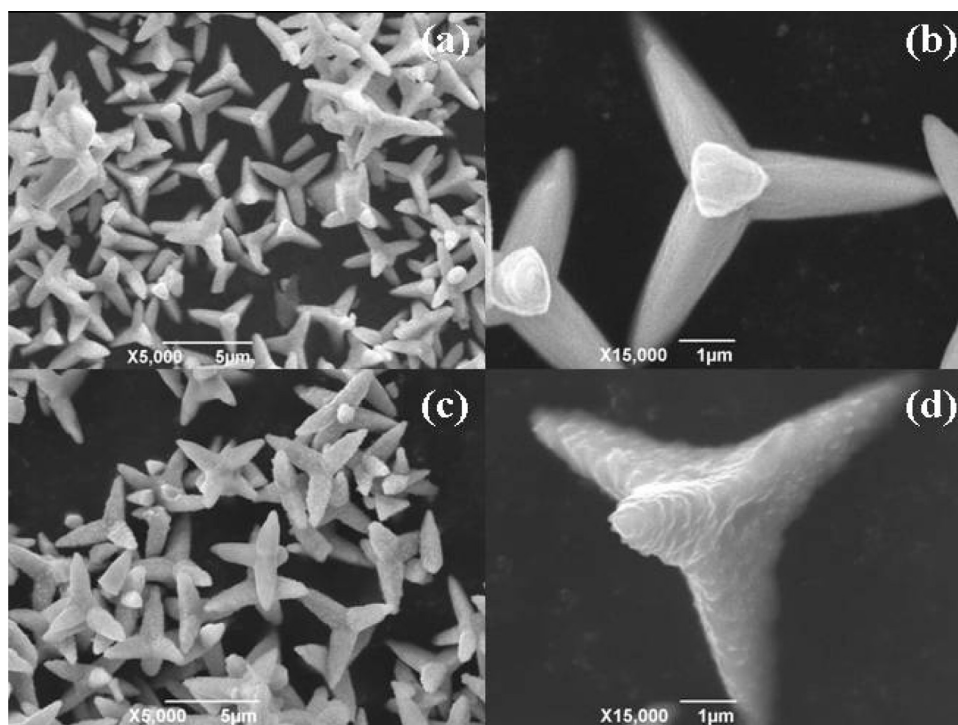


Fig. 2. SEM images of the samples: (a) and (b) Ag_3PO_4 , (c) and (d) 2.0 wt% $\text{Co}_3\text{O}_4/\text{Ag}_3\text{PO}_4$ (673 K).

3. Results and discussion

3.1. Characterization of the samples

Fig. 1 shows the XRD patterns of the samples. As shown in Fig. 1(a), all patterns of pure Ag_3PO_4 sample can be indexed to the body-centered cubic (bcc) structure of Ag_3PO_4 (JCPDS No. 06-0505), and the strong and sharp peaks indicate the high crystallinity of the Ag_3PO_4 sample. In pure Co_3O_4 , the characteristic diffraction peaks can be assigned to the spinel type cubic structure of Co_3O_4 with Fd3m space group (JCPDS No. 42-1467) [40]. In the $\text{Co}_3\text{O}_4/\text{Ag}_3\text{PO}_4$ composites, the main diffraction peaks and their intensities have no obvious changes compared with that of pure Ag_3PO_4 , indicating the crystal structure of samples keeps stable, while the characteristic peaks of Co_3O_4 are not observed owing to the relatively low content of Co_3O_4 . As shown in Fig. 1(b), for the sample calcinated at 473 K, there are only Ag_3PO_4 peaks confirmed. With increasing of temperature, three additional peaks related to metallic Ag at 38.2° , 44.4° and 64.5° are gradually observed, matching well with the (200), (220) and (311) planes of the face-centered cubic structure Ag (JCPDS No. 04-0783), indicating the Ag_3PO_4 particles begin to decompose to produce metallic Ag with increasing of temperature [41]. Furthermore, the relative intensities of main diffraction peaks of $\text{Co}_3\text{O}_4/\text{Ag}_3\text{PO}_4$ calcinated at 773 K have obvious changes, indicating morphology of sample may have changed dramatically, which can be confirmed by SEM observations (see Supporting Information Fig. S1). Besides, we had calculated the intensity ratios of the (222)/(200) and (222)/(110) peaks of the Ag_3PO_4 tetrapods and irregular Ag_3PO_4 crystals according Supporting Information Fig. S2, and the intensity ratios (1.30 and 2.11) of Ag_3PO_4 tetrapods are remarkably higher than those (1 and 1.31) of irregular Ag_3PO_4 particles, suggesting that the surfaces of Ag_3PO_4 are dominated by {111} planes [39].

The morphology of the as-prepared samples was characterized by SEM. The SEM images of Ag_3PO_4 in Fig. 2(a) and (b) clearly show the samples are composed of uniform three-dimensional tetrapod Ag_3PO_4 microcrystals with a smooth surface, whose arms are tri-

angular prisms stretching out in four {111} directions. The four triangular prism arms are 2–3 μm in length and about 900 nm in side length. The side planes of the each triangular-prism are enclosed by {111} facets. As shown in Fig. 2(c) and (d), it can be clearly seen that Co_3O_4 particles are tightly attached on the surface of Ag_3PO_4 in 2.0 wt% $\text{Co}_3\text{O}_4/\text{Ag}_3\text{PO}_4$ (673 K) composite, which indicates the intimate contact between Co_3O_4 and Ag_3PO_4 . Pure Co_3O_4 particles are spherical with diameters of 30–50 nm (Supporting Information Fig. S3(a)) and irregular Ag_3PO_4 crystals are spherical with the particle size of 300–1000 nm (Supporting Information Fig. S3(b)). The energy-dispersive X-ray spectrometry (EDS) analysis of 2.0 wt% $\text{Co}_3\text{O}_4/\text{Ag}_3\text{PO}_4$ (673 K) composite is shown in Supporting Information Fig. S4, and O, P, Ag and Co as major elements are detected from the sample. The atomic ratio of Ag:P:Co is 3.192:1:0.108, which is close to the theoretical value of 3:1:0.104 for 2.0 wt% $\text{Co}_3\text{O}_4/\text{Ag}_3\text{PO}_4$, further identifying the existence of Co_3O_4 and Ag_3PO_4 . Moreover, the atomic ratio of Ag and P is more than 3. Based on the assumption that the atomic ratio of Ag and P was 3:1 in pure Ag_3PO_4 , the extra Ag content would be contributed by metallic Ag [37].

It is well known that the high surface area is beneficial for the adsorption and photocatalytic activity, the BET experiment ruled out the contribution of surface area. The specific surface area of pure Ag_3PO_4 is $4.433 \text{ m}^2/\text{g}$. After loading Co_3O_4 on Ag_3PO_4 particles, the specific surface area of 2.0 wt% $\text{Co}_3\text{O}_4/\text{Ag}_3\text{PO}_4$ (673 K) increases to $5.104 \text{ m}^2/\text{g}$.

The FT-IR spectra of Ag_3PO_4 and $\text{Co}_3\text{O}_4/\text{Ag}_3\text{PO}_4$ composites are shown in Fig. 3. For pure Co_3O_4 , the strong peaks at 657 and 556 cm^{-1} can be observed, which can be attributed to the characteristic peaks of spinel Co_3O_4 [42]. The former peak at 657 cm^{-1} is belonged to the stretching vibration mode of M–O in which M is Co^{2+} and is tetrahedrally coordinated. While the band at 556 cm^{-1} can be assigned to the M–O in which M is Co^{3+} and so coordinates octahedrally. For pure Ag_3PO_4 , the observed strong peaks at 547 and 943 cm^{-1} are attributed to the characteristic peaks of PO_4^{3-} [43]. In addition, characteristic peaks corresponding to Co_3O_4 and Ag_3PO_4 appear in $\text{Co}_3\text{O}_4/\text{Ag}_3\text{PO}_4$ composites, and the

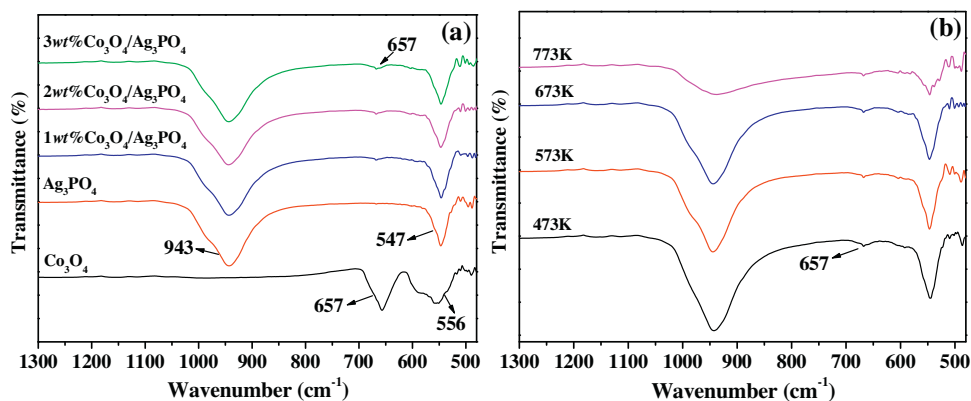


Fig. 3. FT-IR spectra of the samples: (a) Co_3O_4 , Ag_3PO_4 and $\text{Co}_3\text{O}_4/\text{Ag}_3\text{PO}_4$ composites with different Co_3O_4 content calcined at 673 K, (b) the 2.0 wt% $\text{Co}_3\text{O}_4/\text{Ag}_3\text{PO}_4$ composites calcined at different temperature.

relative intensity of the peaks of Co_3O_4 increases with the increase of Co_3O_4 content in composites (Fig. 3(a)). As shown in Fig. 3(b), in the range of experimental temperatures (473 ~ 773 K), the peak of Co_3O_4 appeared in the $\text{Co}_3\text{O}_4/\text{Ag}_3\text{PO}_4$ composites, indicating the formation and stability of Co_3O_4 in the experimental temperatures (473 ~ 773 K). However, the relative intensity of peaks of Ag_3PO_4 become weaker significantly at 773 K, further suggesting Ag_3PO_4 decomposes.

The color of pure Ag_3PO_4 and Co_3O_4 powders are yellow and black, respectively. The color of the $\text{Co}_3\text{O}_4/\text{Ag}_3\text{PO}_4$ composite powders is dark green and becomes darker by enhancing the Co content or increasing the calcination temperature. Fig. 4 shows UV–vis absorption spectra of samples. Pure Ag_3PO_4 can absorb visible light with wavelengths shorter than 530 nm. Co_3O_4 presents a wide and strong light absorption in the whole UV–vis range of 200 ~ 800 nm, and two absorption peaks are observed at ~720 nm and ~390 nm which are assigned to ligand-metal charge transfer of $\text{O}(\text{II}) \rightarrow \text{Co}(\text{III})$ and $\text{O}(\text{II}) \rightarrow \text{Co}(\text{II})$, respectively [44,45]. As Co_3O_4 was introduced into Ag_3PO_4 , the ability of light absorption is enhanced greatly, especially in the range of 500 ~ 800 nm, and the absorption intensity of $\text{Co}_3\text{O}_4/\text{Ag}_3\text{PO}_4$ composite increases with increasing Co content. Meanwhile, the increase of light absorption in the range of 200 ~ 500 nm should be mainly attributed to the effects of calcination of Ag_3PO_4 (see Supporting Information Fig. S5). The UV–vis absorption spectra of 2.0 wt% $\text{Co}_3\text{O}_4/\text{Ag}_3\text{PO}_4$ composites calcined at different temperature are displayed in Fig. 4(b). The absorption intensity of $\text{Co}_3\text{O}_4/\text{Ag}_3\text{PO}_4$ composite increases with increasing calcination temperature in the range of 473 ~ 673 K, which may be attributed to the decreasing defects of the Ag_3PO_4 crystals and the increasing amount of metallic Ag nanoparticles during the calcination process [46]. However, when the calcination temperature gets up to 773 K, the shape of UV–vis absorption spectrum have changed, which may be attributed to the melting and sintering of Ag_3PO_4 , which can be identified by Supporting Information Fig. S1.

According to the plot of $(F(R)h\nu)^{1/2}$ vs $h\nu$, the band gaps (E_g) of Ag_3PO_4 and Co_3O_4 were estimated to be 2.55 and 1.90 eV, respectively (Fig. S6, Supporting Information). The band structure of Ag_3PO_4 and Co_3O_4 can be estimated according to the empirical equations [47] as shown below:

$$E_{\text{VB}} = \chi - E_e + 0.5E_g$$

$$E_{\text{CB}} = E_{\text{VB}} - E_g$$

where E_{VB} and E_{CB} are the valence and conduction band edge potentials, respectively; χ is the absolute electronegativity of the semiconductor, expressed as the geometric mean of the absolute electronegativity of the constituent atoms, and defined as the arith-

Table 1

Calculation of the CB and VB potentials of Ag_3PO_4 and Co_3O_4 .

	χ	E_g (eV)	E_{CB} (eV)	E_{VB} (eV)
Ag_3PO_4	5.96	2.55	0.18	2.73
Co_3O_4	5.90	1.90	0.45	2.35

metic mean of the atomic electro affinity and the first ionization energy; E_e is the energy of free electrons on the hydrogen scale (about 4.5 eV vs NHE); E_g was the band gap energy of the semiconductor. Thus, the calculated values of the CB and VB potentials of Ag_3PO_4 and Co_3O_4 are listed in Table 1.

The surface chemical compositions and chemical states of the elements of 2.0 wt% $\text{Co}_3\text{O}_4/\text{Ag}_3\text{PO}_4$ (673 K) composite were analyzed by XPS (Fig. 5). Fig. 5(a) displays the full XPS spectrum of the sample. The photoelectron peaks of Ag, O, P, Co and C elements are clearly observed, which is consistent with the EDS result. As shown in Fig. 5(b), the Ag 3d peaks of the $\text{Co}_3\text{O}_4/\text{Ag}_3\text{PO}_4$ sample can be separated as the Ag^+ and Ag^0 peaks. The strong peaks at 367.8 and 373.8 eV can be assigned to Ag^+ of Ag_3PO_4 , while the weak peaks at 369.0 and 375.0 eV belong to the metallic Ag^0 [48], indicating that metallic Ag was formed on the surface of Ag_3PO_4 photocatalyst during the calcination process. Considering that no diffraction peaks of Ag in XRD are observed, the detected metallic Ag should be tiny and well dispersed on the surface of Ag_3PO_4 [37]. Fig. 5(c) shows the Co 2p XPS spectrum of the composite. The Co 2p_{1/2} and Co 2p_{3/2} binding energies were found to be at 796.2 eV and 780.9 eV, and the spin energy separation was 15.3 eV [44,45]. In Fig. 5(d), a broad peak in the range of 130 to 136 eV appears to be attributable to the P element in PO_4^{3-} [48]. For the O 1s (Fig. 5(e)), the peak at 530.6 eV is assigned to the crystal lattice oxygen, while the peak at 532.2 eV is related to adsorbed oxygen [49], which favours the degradation of organic pollutants in water.

3.2. Photocatalytic tests

Photocatalytic tests of samples were evaluated by photodegradation of MB under visible light irradiation ($\lambda > 400$ nm), and the results are shown in Fig. 6. A pseudo-first-order kinetic model was employed to fit the degradation data by using the equation [17]: $-\ln(C/C_0) = kt$, where k is the apparent reaction rate constant (min^{-1}), and C_0 and C are the adsorption equilibrium concentration and concentration at reaction time t of MB, respectively. Fig. 6(a) shows the remaining MB in solution after adsorption equilibrium and the MB degradation (C/C_0) with the irradiation time. After adsorption equilibrium, 86.8%, 94.9% and 91.6% of MB remain in the solution with the Co_3O_4 , tetrapod Ag_3PO_4 and 2.0 wt% $\text{Co}_3\text{O}_4/\text{Ag}_3\text{PO}_4$ (673 K) photocatalysts, respectively. By modification with Co_3O_4 ,

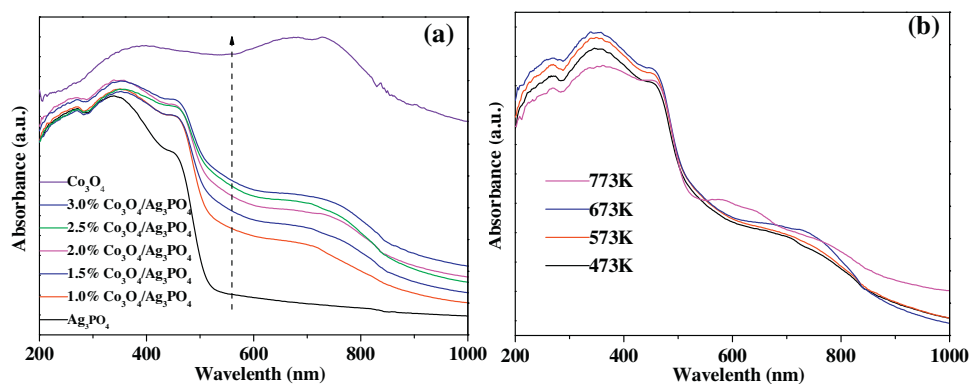


Fig. 4. UV–vis absorption spectra of the samples: (a) Co_3O_4 , Ag_3PO_4 and $\text{Co}_3\text{O}_4/\text{Ag}_3\text{PO}_4$ composites with different Co_3O_4 content calcined at 673K, (b) the 2.0 wt% $\text{Co}_3\text{O}_4/\text{Ag}_3\text{PO}_4$ composites calcined at different temperature.

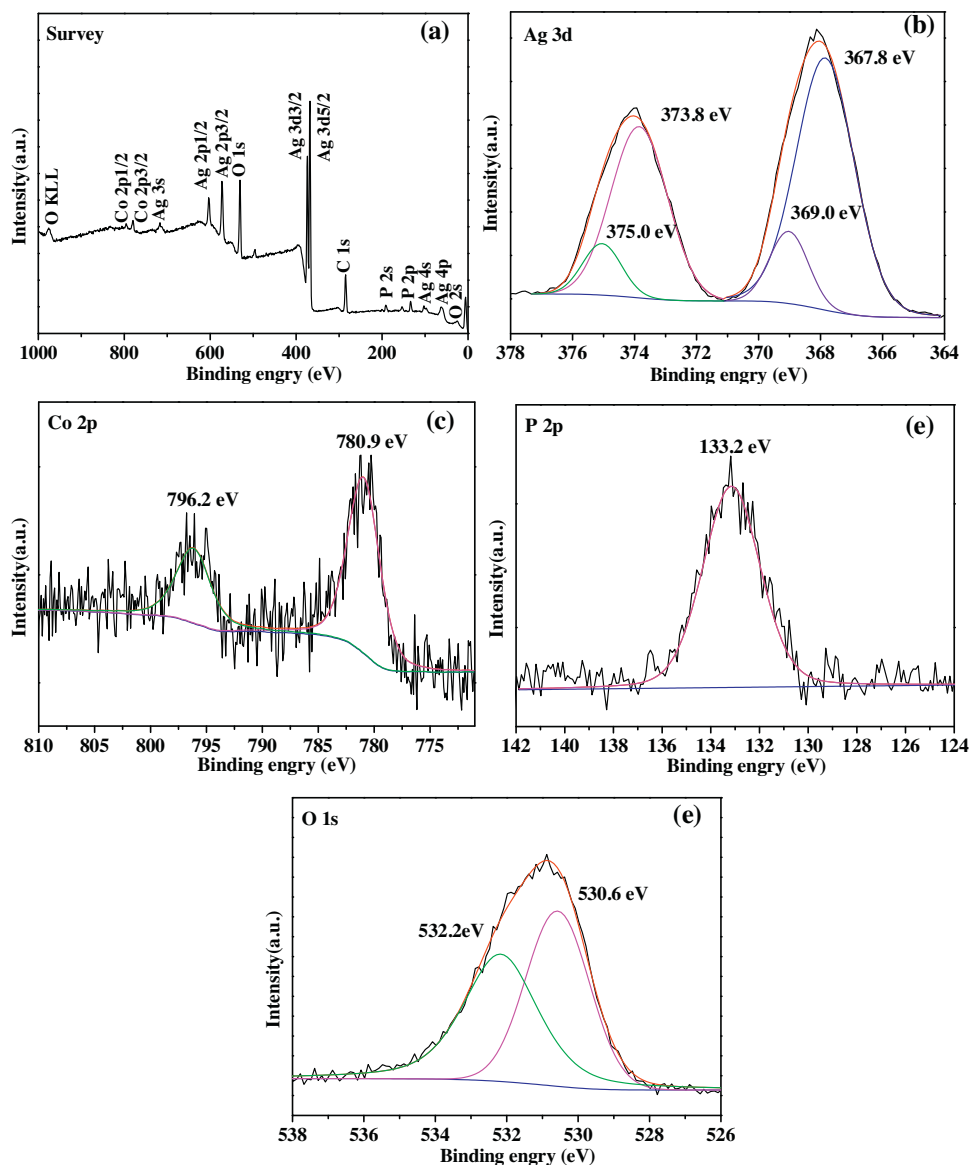


Fig. 5. XPS spectra of 2.0 wt% $\text{Co}_3\text{O}_4/\text{Ag}_3\text{PO}_4$ (673 K) sample: (a) survey scan, (b) Ag 3d, (c) Co 2p, (d) P 2p, and (e) O 1s.

the adsorptivity of Ag_3PO_4 to MB is enhanced, which benefits from the higher specific surface area and is beneficial to the photodecomposition of MB. It can be seen the direct photodegradation of MB is

not obvious, suggesting MB self-photolysis is negligible in the process of photocatalysis. Compared with Co_3O_4 , all Ag_3PO_4 samples exhibit excellent catalytic activities, and the $\text{Co}_3\text{O}_4/\text{Ag}_3\text{PO}_4$ shows

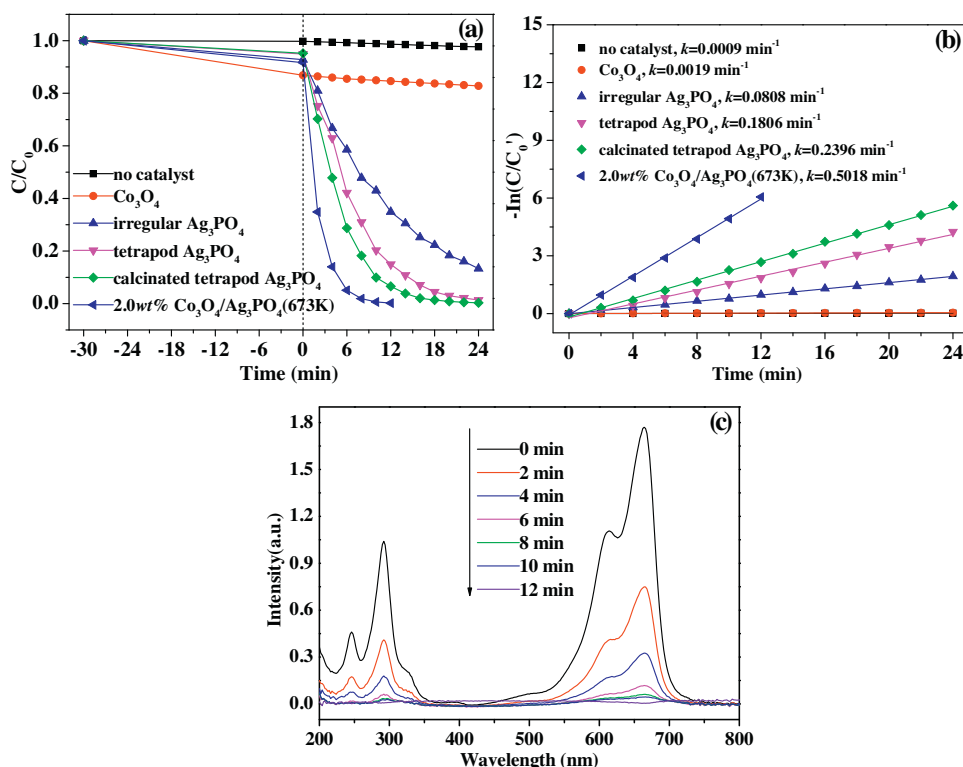


Fig. 6. (a) Photocatalytic degradation curves of MB over as-prepared samples under the visible light irradiation ($>400 \text{ nm}$); (b) Apparent rate constants for the photodegradation of MB over samples; (c) UV-visible spectra of MB at different visible irradiation times in the presence of 2.0 wt% $\text{Co}_3\text{O}_4/\text{Ag}_3\text{PO}_4$ (673 K).

the highest photocatalytic activity. The k of 2.0 wt% $\text{Co}_3\text{O}_4/\text{Ag}_3\text{PO}_4$ (673 K) is 0.5018 min^{-1} , which is 2.78 and 264.1 times as high as that of pure Ag_3PO_4 tetrapods (0.1806 min^{-1}) and pure Co_3O_4 (0.0019 min^{-1}). Meanwhile, it can be clearly seen that the Ag_3PO_4 tetrapods shows better photocatalytic activities than that of irregular Ag_3PO_4 particles (0.0808 min^{-1}), and the k of Ag_3PO_4 tetrapods is about 2.24 times higher than that of irregular Ag_3PO_4 , which is due to the higher surface energy and more active sites of $\{111\}$ facets. To further investigate the contribution of Co_3O_4 and Ag, MB degradation activity of the calcined tetrapod Ag_3PO_4 (673 K) without Co_3O_4 (0.2396 min^{-1}) was also tested, and it shows an evident decrease compared to that of 2.0 wt% $\text{Co}_3\text{O}_4/\text{Ag}_3\text{PO}_4$ (673 K); hence it illustrates that it is Co_3O_4 rather than Ag that plays the core role in the process.

The effects of the Co_3O_4 content and calcination temperature on the photocatalytic activity were also investigated. As exhibited in Fig. 7(a), the photodegradation efficiency the heterostructured samples are greatly dependent on the content of Co_3O_4 . At first, the activity for degradation MB increases with increasing loading of Co_3O_4 , and these results simultaneously demonstrate that the introduction of Co_3O_4 could effectively improve photocatalytic activity of Ag_3PO_4 . The number of $\text{Co}_3\text{O}_4/\text{Ag}_3\text{PO}_4$ heterojunctions increases with the increasing of Co_3O_4 content and a larger number of electron-hole pairs within the space charge region are efficiently separated by $\text{Co}_3\text{O}_4/\text{Ag}_3\text{PO}_4$ heterogenous junction. However, a further increase in the amount of Co_3O_4 results in a decrease in the photocatalytic activity, which is likely due to the “shielding effect” of Co_3O_4 . Excessive Co_3O_4 clusters cover the active sites on the Ag_3PO_4 surface and leads to a decrease of the absorption of the incident light on Ag_3PO_4 . Therefore, an appropriate content of Co_3O_4 is crucial to achieve optimal photocatalytic performance. Fig. 7(b) shows the photocatalytic activities of 2.0 wt% $\text{Co}_3\text{O}_4/\text{Ag}_3\text{PO}_4$ composite calcined at different temperature under visible light irradiation. The photodegradation efficiency

first increases and then decreases with rising calcination temperature, and $\text{Co}_3\text{O}_4/\text{Ag}_3\text{PO}_4$ calcined at 673 K displays the highest activity. With increasing of temperature, the crystallinity of Co_3O_4 is improved [50], and the contact between Co_3O_4 and Ag_3PO_4 becomes more and more intimate. Highly crystallized structure always favors migration of electron-hole pairs as compared to the amorphous structure, and the intimate contact between Co_3O_4 and Ag_3PO_4 makes for the formation of heterojunction, so as to high photocatalytic activity. Meanwhile, the Ag_3PO_4 particles decompose to produce more and more metallic Ag with increasing of temperature. It is reported that Ag^0 in Ag/silver halide structures is beneficial to the photocatalytic efficiency in organic dye decomposition [46,51]. When the temperature increases to 773 K, the Ag_3PO_4 decomposes rapidly (see Fig. 1(b)) and the active $\{111\}$ facets of Ag_3PO_4 disappears (see Supporting Information Fig. S1), which conduces to the sharp decline in photocatalytic activity.

Besides the excellent photocatalytic efficiency, the reusability and stability of the as-synthesized photocatalyst was studied by the circulating runs, and they were performed five times on 2.0 wt% $\text{Co}_3\text{O}_4/\text{Ag}_3\text{PO}_4$ (673 K) and pure Ag_3PO_4 samples. The corresponding results are shown in Fig. 8. The photocatalytic performance of pure Ag_3PO_4 shows a significant reduction during the repeated photocatalytic reactions, but the photocatalytic activity of the $\text{Co}_3\text{O}_4/\text{Ag}_3\text{PO}_4$ do not show significant loss after five cycling runs of photodegradation of MB, which indicate that the $\text{Co}_3\text{O}_4/\text{Ag}_3\text{PO}_4$ heterojunction photocatalyst is an efficient visible light driven photocatalyst, good reusability, and stability for potential practical applications in wastewater treatment.

At present, we have identified two possible reasons to explain the enhanced stabilities of $\text{Co}_3\text{O}_4/\text{Ag}_3\text{PO}_4$ heterocrystals compared with pure Ag_3PO_4 crystals. First, there are the different solubility of pure Ag_3PO_4 and the $\text{Co}_3\text{O}_4/\text{Ag}_3\text{PO}_4$ heterocatalysts in the present system. The Ag_3PO_4 catalyst possesses a relatively high solubility of about 0.02 g L^{-1} in aqueous solution (25°C) [52], While Co_3O_4

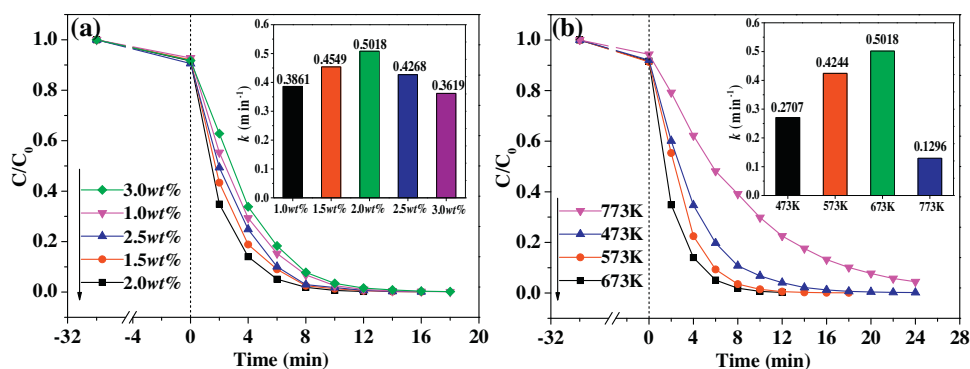


Fig. 7. Photocatalytic degradation curves of MB over samples: (a) $\text{Co}_3\text{O}_4/\text{Ag}_3\text{PO}_4$ composites with different Co_3O_4 content calcined at 673 K, (b) 2.0 wt% $\text{Co}_3\text{O}_4/\text{Ag}_3\text{PO}_4$ (673 K) composites calcined at different temperature.

nanoparticles possess a much lower solubility (0.00011 g L^{-1} , 20°C) [53], which are in intimate contact with the outer surface of the Ag_3PO_4 crystals, preventing the dissolution of the Ag_3PO_4 core-crystals. Thus, their structural stabilities during the photocatalytic process have been greatly enhanced.

Second, the metallic Ag in $\text{Co}_3\text{O}_4/\text{Ag}_3\text{PO}_4$ composites can effectively protect Ag_3PO_4 semiconductors to avoid their photoreduction ($\text{Ag}^+ + \text{e}^- \rightarrow \text{Ag}$). The measurements of the used samples were further conducted by the UV–vis absorption spectrum, XRD and XPS (Fig. S7 and Fig. S8, Supporting Information). As shown in Fig. S7, it is observed that obvious metallic Ag^0 is formed after the first cycling run in UV–vis absorption spectrum, XRD and XPS, which suggests that part of the Ag_3PO_4 has decomposed to Ag^0 . It is well known that Ag_3PO_4 is easily photocorroded by the photo-generated electrons and decomposed to weakly active Ag^0 , leading to the instability in its visible-light photocatalytic activity [54]. As the photocatalytic reaction mainly occurs on the active site on the surface of Ag_3PO_4 , this kind of weakly active Ag^0 are mainly produced on the active sites of the Ag_3PO_4 surfaces in the photocatalytic process, which would cover the active sites of Ag_3PO_4 and shield the light absorption [55,56], thus resulting in decrease of photocatalytic efficiency. However, it can be seen from Fig. S8(a) and (b), there are inappreciable changes in the UV–vis absorption spectrum and phase structure of $\text{Co}_3\text{O}_4/\text{Ag}_3\text{PO}_4$ composites after 1 recycling run. As seen in Fig. S8(c), the surface content of metallic Ag^0 in Ag species on fresh and used $\text{Co}_3\text{O}_4/\text{Ag}_3\text{PO}_4$ composites are 0.159 and 0.163, respectively, and the Co 2p peaks of $\text{Co}_3\text{O}_4/\text{Ag}_3\text{PO}_4$ composites have no obvious change before and after photodegradation experiments. These results indicate that the $\text{Co}_3\text{O}_4/\text{Ag}_3\text{PO}_4$ heterojunction photocatalyst give rise to structural stability than bare Ag_3PO_4 . Why? These metallic Ag^0 particles produced in the

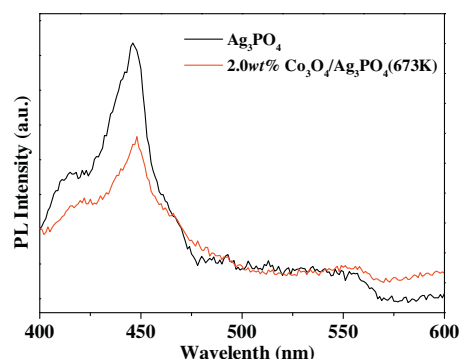


Fig. 9. Photoluminescence spectra of Ag_3PO_4 and 2.0 wt% $\text{Co}_3\text{O}_4/\text{Ag}_3\text{PO}_4$ (673 K) composite.

calcination process are very tiny and well dispersed on the surface of Ag_3PO_4 which can serve as excellent acceptors to trap for photoexcited electrons; hence, the photoinduced electrons could be quickly transferred to Ag^0 nanoparticles [37] and consumed by subsequent reaction (Section 3.3), which prevent further formation of more Ag^0 specie during the photocatalysis.

3.3. Photocatalytic mechanism

The PL spectrum is useful for revealing the mitigation, transfer, and recombination processes of the photogenerated electron-hole pairs in a semiconductor. In general, a lower PL intensity indicates lower recombination of charge carriers, leading to higher photocatalytic activity. The room temperature PL emission spectra of pure Ag_3PO_4 and 2.0 wt% $\text{Co}_3\text{O}_4/\text{Ag}_3\text{PO}_4$ (673 K) composite are shown in Fig. 9. The PL spectrum of Ag_3PO_4 has a typical broad band profile with the maximum emissions located in 445 nm, which is mainly caused by the recombination electron-hole pairs directly involves a cluster-to-cluster charge transfer, i.e., between $[\text{AgO}_4-\text{PO}_4]$ clusters and $[\text{AgO}_4-\text{AgO}_4]$ clusters [57]. Meanwhile, a similar PL spectrum is obtained for 2.0 wt% $\text{Co}_3\text{O}_4/\text{Ag}_3\text{PO}_4$ (673 K); nevertheless, the overall emission intensity is obviously reduced compared with that of pure Ag_3PO_4 . This indicated recombination of charge carriers on $\text{Co}_3\text{O}_4/\text{Ag}_3\text{PO}_4$ composites is inhibited and is beneficial for the improvement of photocatalytic activity.

In order to deduce the migration path of the photogenerated electrons and holes in the composite, the active species trapping experiments were conducted. Fig. 10 displays the photocatalytic process of 2.0 wt% $\text{Co}_3\text{O}_4/\text{Ag}_3\text{PO}_4$ (673 K) with different quenchers (isopropyl alcohol (IPA), triethanolamine (TEOA), and p-benzoquinone (BQ), which are known as effective $\cdot\text{OH}$, holes, and $\text{O}_2^{\cdot-}$ scavengers, respectively) and purging

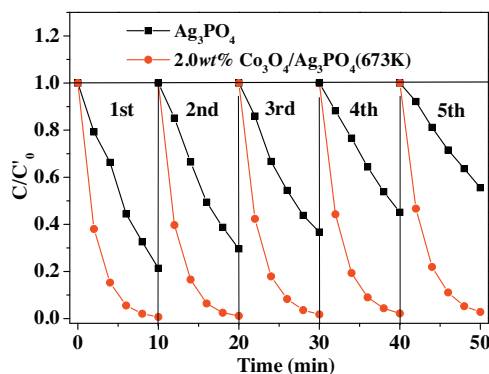


Fig. 8. Cycling runs for the photocatalytic degradation of MB over pure Ag_3PO_4 and 2.0 wt% $\text{Co}_3\text{O}_4/\text{Ag}_3\text{PO}_4$ (673 K) composite under visible light irradiation.

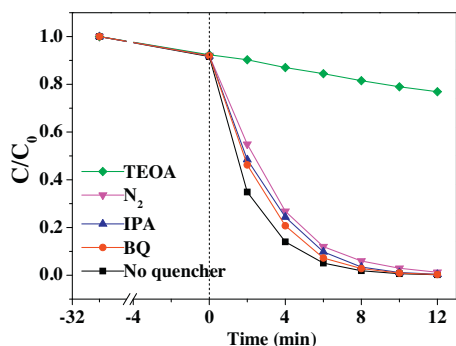


Fig. 10. Plots of photogenerated active species trapped in the system of photodegradation of MB by 2.0 wt% $\text{Co}_3\text{O}_4/\text{Ag}_3\text{PO}_4$ (673 K) under visible light irradiation.

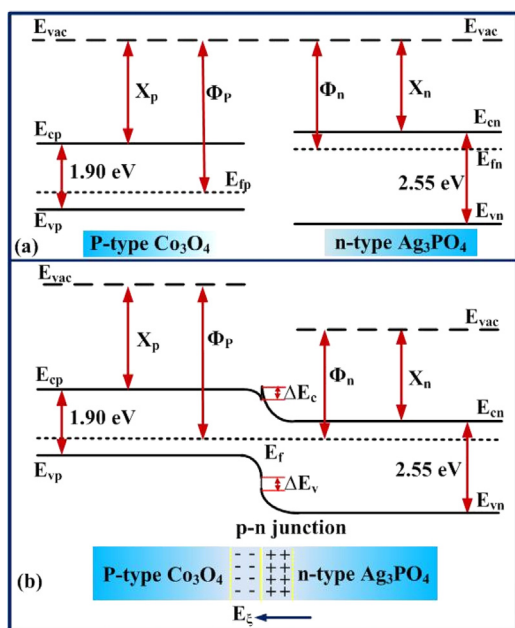


Fig. 11. (a) The energy band structures of Co_3O_4 and Ag_3PO_4 before formation of heterojunction and (b) the energy band structures of $p\text{-Co}_3\text{O}_4/n\text{-Ag}_3\text{PO}_4$ heterojunction at equilibrium (E_{vac} : vacuum level; E_f : Fermi level; Φ : work function; X : electron affinity).

N_2 . It can be found that the photodegradation rates decrease in the order: TEOA (0.0158 min^{-1}) < purging N_2 (0.361 min^{-1}) < IPA (0.4577 min^{-1}) < BQ (0.4802 min^{-1}), indicating that h^+ is the most important reactive species, O_2 has some positive effect, and $\bullet\text{OH}$ and $\text{O}_2^{\bullet-}$ are the minor reactive species in the photocatalytic process.

The enhanced photocatalytic performance of $\text{Co}_3\text{O}_4/\text{Ag}_3\text{PO}_4$ composite can be explained by assuming the formation of $p\text{-}n$ junction between p -type Co_3O_4 and n -type Ag_3PO_4 semiconductors. On the basis of the energy band structures of semiconductor Co_3O_4 and Ag_3PO_4 crystals, it can be seen that before contacting of p -type Co_3O_4 with n -type Ag_3PO_4 , the conduction band edge of p -type Co_3O_4 is lower than that of n -type Ag_3PO_4 , and the Fermi level of the Co_3O_4 is also lower than that of the Ag_3PO_4 , as shown in Fig. 11(a). After contact of p -type Co_3O_4 with n -type Ag_3PO_4 , the Fermi level of Co_3O_4 is raised up, while the Fermi level of Ag_3PO_4 is lowered until an equilibrium state is formed as shown in Fig. 11(b). The $p\text{-}n$ junction at the interface between Co_3O_4 and Ag_3PO_4 crystals is formed, while an inner electric field (E_ξ) from n -type Ag_3PO_4 to p -type Co_3O_4 is established at the equilibrium. A large number of p -type Co_3O_4 nanoparticles are tightly assembled on the surface of n -type Ag_3PO_4 crystals. Thus a large number of nano $p\text{-}n$ junctions

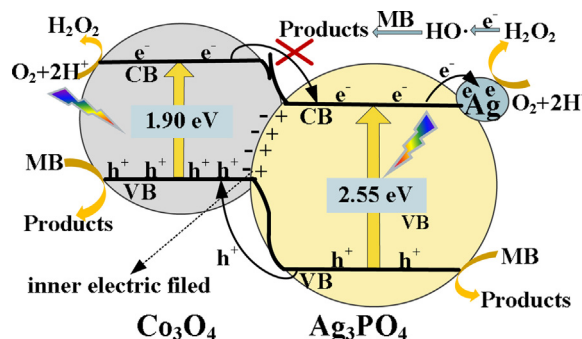


Fig. 12. Photocatalytic mechanism scheme of the $\text{Co}_3\text{O}_4/\text{Ag}_3\text{PO}_4$ composite.

tions are formed on the surface of Ag_3PO_4 nanocrystals. As shown in Fig. 12, under visible light irradiation, both Ag_3PO_4 and Co_3O_4 can be excited to generate photogenerated electrons (e^-) and holes (h^+). According to the position of band energy in Fig. 12, the excited electrons on the CB of the p -type Co_3O_4 cannot be transferred to that of the n -type Ag_3PO_4 due to the energy barrier existing at the interface between Co_3O_4 crystallites and Ag_3PO_4 crystallites [58]. However, the photogenerated holes on VB of n -type Ag_3PO_4 can be migrated to that of p -type Co_3O_4 easily. Such a migration of photogenerated carriers can be promoted by the internally formed electric field. Therefore, the photogenerated electrons and holes of n -type Ag_3PO_4 can be separated effectively by the $p\text{-}n$ junctions formed between the p -type Co_3O_4 and n -type Ag_3PO_4 interface, and the recombination of electron-hole pairs can be substantially retarded. On the other hand, it is well known that metallic Ag^0 can serve as excellent acceptors, trap for photoexcited electrons and they are capable of storing electrons [59]. Hence, the photoinduced electrons on CB of Ag_3PO_4 can be quickly transferred to Ag^0 particles instead of remain in Ag_3PO_4 lattice, which further facilitates charges separation in Ag_3PO_4 . This entire process would facilitate charge separation and improve photocatalytic activity. Subsequently, holes on the valence band (VB) of Co_3O_4 and Ag_3PO_4 could oxidize MB directly. Meanwhile, the accumulated electrons on Ag^0 nanoparticles and the CB of Co_3O_4 can reduce dissolved O_2 adsorbed on the surface of the composite semiconductors to H_2O_2 [52], and H_2O_2 reacts with electrons in succession to produce active $\bullet\text{OH}$ radicals, which are then involved in the photocatalytic degradation reaction of MB.

4. Conclusions

In summary, novel tetrapod Ag_3PO_4 microcrystals with exposed $\{111\}$ facets and $\text{Co}_3\text{O}_4/\text{Ag}_3\text{PO}_4$ heterojunction photocatalysts were successfully prepared via a facile precipitation method and an impregnation method, respectively. The 2.0 wt% $\text{Co}_3\text{O}_4/\text{Ag}_3\text{PO}_4$ (673 K) sample demonstrated the highest photocatalytic activity for photodegradation of MB under visible light. The improved photocatalytic performance could be mainly attributed to accelerated electron-hole separation by $p\text{-}n$ junctions in $\text{Co}_3\text{O}_4/\text{Ag}_3\text{PO}_4$ heterojunction, and the enhanced structural stabilities may be due to the protection of insoluble Co_3O_4 and the effect of Ag^0 on the surface of Ag_3PO_4 . Moreover, h^+ played the major role in the MB decolorization. The $\text{Co}_3\text{O}_4/\text{Ag}_3\text{PO}_4$ composite could be used as a promising photocatalyst in the applications of environmental remediation. Furthermore, this strategy could also be adapted for the preparation of other Ag-based semiconductor heterostructures, such as $\text{Co}_3\text{O}_4/\text{Ag}_2\text{S}$, $\text{Co}_3\text{O}_4/\text{Ag}_2\text{MoO}_4$, $\text{Co}_3\text{O}_4/\text{Ag}_2\text{WO}_4$, $\text{Co}_3\text{O}_4/\text{AgVO}_3$, etc.

Acknowledgments

This work was supported by the National Natural Science Foundation of China (Nos. 21476183, 21176199, 21306150 and 51372201), the Specialized Research Fund for the Doctoral Program of Higher Education of China (No. 20136101110009), the Shaanxi Provincial Research Foundation for Basic Research, China (Nos. 2015JM5159), and the Research and Development Project of Shaanxi Institute of Technology (Gfy15-20).

Appendix A. Supplementary data

Supplementary data associated with this article can be found, in the online version, at <http://dx.doi.org/10.1016/j.apcatb.2015.08.045>.

References

- [1] A. Fujishima, K. Honda, *Nature* 238 (1972) 37–38.
- [2] C.C. Chen, W. Ma, J.C. Zhao, *Chem. Soc. Rev.* 39 (2010) 4206–4219.
- [3] Z.G. Yi, J.H. Ye, N. Kikugawa, T. Kako, S.X. Ouyang, H. Stuart-Williams, H. Yang, J.C. Cao, W.J. Luo, Z.S. Li, Y. Liu, R.L. Withers, *Nat. Mater.* 9 (2010) 559–564.
- [4] X. Hua, Y.J. Jin, K. Wang, N. Li, H.Q. Liu, M.D. Chen, S.S. Paul, Y. Zhang, X.D. Zhao, F. Teng, *Catal. Commun.* 52 (2014) 49–52.
- [5] Z.M. Yang, Y. Tian, G.F. Huang, W.Q. Huang, Y.Y. Liu, C. Jiao, Z. Wan, X.G. Yan, A.L. Pan, *Mater. Lett.* 116 (2014) 209–211.
- [6] Y.P. Bi, S.X. Ouyang, N. Umezawa, J.Y. Cao, J.H. Ye, J. Am. Chem. Soc. 133 (2011) 6490–6492.
- [7] Z.B. Jiao, Y. Zhang, H.C. Yu, G.X. Lu, J.H. Ye, Y.P. Bi, *Chem. Commun.* 49 (2013) 636–638.
- [8] M. Li, M.D. Chen, J. Wang, F. Teng, *CrystEngComm* 16 (7) (2014) 1237–1240.
- [9] H. Wang, L. He, L.H. Wang, P.F. Hu, L. Guo, X.D. Han, J.H. Li, *CrystEngComm* 14 (2013) 8342–8344.
- [10] Y.K. Jo, I.Y. Kim, J.M. Lee, S. Nahm, J.W. Choi, S.J. Hwang, *Mater. Lett.* 114 (2014) 152–155.
- [11] H.G. Yu, G.Q. Cao, F. Chen, X.F. Wang, J.G. Yu, M. Lei, *Appl. Catal. B: Environ.* 160 (2014) 658–665.
- [12] S.N. Zhang, S.J. Zhang, L.M. Song, *Appl. Catal. B: Environ.* 152 (2014) 129–139.
- [13] Y.P. Xie, G.S. Wang, *J. Colloid, Interf. Sci.* 430 (2014) 1–5.
- [14] C.N. Tang, E.Z. Liu, J. Fan, X.Y. Hu, L.M. Kang, J. Wan, *Ceram. Int.* 40 (2014) 15447–15453.
- [15] L.L. Zhang, H.C. Zhang, H. Huang, Y. Liu, Z.H. Kang, *New J. Chem.* 36 (2012) 1541–1544.
- [16] C. Dong, K.L. Wu, M.R. Li, L. Liu, X.W. Wei, *Catal. Commun.* 46 (2014) 32–35.
- [17] Z.M. Yang, G.F. Huang, W.Q. Huang, J.M. Wei, X.G. Yan, Y.Y. Liu, C. Jiao, Z. Wan, A.L. Pan, *J. Mater. Chem. A* 2 (2014) 1750–1756, w Journal.
- [18] Y.H. Yan, H.Y. Guan, S. Liu, R.Y. Jiang, *Ceram. Int.* 40 (2014) 9095–9100.
- [19] G.K. Fu, G.N. Xu, S.P. Chen, L. Lei, M.L. Zhang, *Catal. Commun.* 40 (2013) 120–124.
- [20] S.Y. Wu, H. Zheng, Y.Y. Wu, W. Lin, T.Z. Xu, M. Guan, *Ceram. Int.* 40 (2014) 14613–14620.
- [21] Z.K. Cui, M.M. Si, Z. Zheng, L.W. Mi, W.J. Fa, H.M. Jia, *Catal. Commun.* 42 (2013) 121–124.
- [22] J.Q. Zhang, K. Yu, Y.F. Yu, L.L. Lou, Z.Q. Yang, J.W. Yang, S.X. Liu, *J. Mol. Catal. A: Chem.* 391 (2014) 12–18.
- [23] P.Q. Wang, Y. Bai, P.Y. Luo, J.Y. Liu, *Micro. Nano Lett.* 8 (2013) 340–344.
- [24] P.F. Wang, P.H. Shi, Y.C. Hong, X.J. Zhou, W.F. Yao, *Mater. Res. Bull.* 62 (2015) 24–29.
- [25] Y.M. He, L.H. Zhang, B.T. Teng, M.H. Fan, *Environ. Sci. Technol.* 49 (2015) 649–656.
- [26] X.J. Chen, Y.Z. Dai, X.Y. Wang, J. Guo, T.H. Liu, F.F. Li, J. Hazard. Mater. 292 (2015) 9–18.
- [27] Q.J. Xiang, D. Lang, T.T. Shen, F. Liu, *Appl. Catal. B: Environ.* 162 (2015) 196–203.
- [28] H. Xu, C. Wang, Y.H. Song, J.X. Zhu, Y.G. Xu, J. Yan, Y.X. Song, H.M. Li, *Chem. Eng. J.* 241 (2014) 35–42.
- [29] H.C. Zhang, H. Huang, H. Ming, H.T. Li, L.L. Zhang, Y. Liu, Z.H. Kang, *J. Mater. Chem.* 22 (2012) 10501–10506.
- [30] M. Casas-Cabanas, G. Binotto, D. Larcher, A. Lecup, V. Giordani, J.M. Tarascon, *Chem. Mater.* 21 (2009) 1939–1947.
- [31] M.C. Long, W.M. Cai, J. Cai, B.X. Zhou, X.Y. Chai, Y.H. Wu, *J. Phys. Chem. B* 110 (2006) 20211–20216.
- [32] S.A. Makhlof, Z.H. Bakr, K.I. Aly, M.S. Moustafa, *Superlattices Microst.* 64 (2013) 107–117.
- [33] Q. Xiao, J. Zhang, C. Xiao, X.K. Tan, *Catal. Commun.* 9 (2008) 1247–1253.
- [34] L. Zhang, Y. He, P. Ye, W. Qin, Y. Wu, T. Wu, *Mat. Sci. Eng. B* 178 (2013) 45–52.
- [35] C.C. Han, L. Ge, C.F. Chen, Y.J. Li, X.L. Xiao, Y.N. Zhang, L.L. Guo, *Appl. Catal. B: Environ.* 147 (2014) 546–553.
- [36] C.W. Tan, G.Q. Zhu, M. Hojamberdiev, K. Okada, J. Liang, X.C. Luo, P. Liu, Y. Liu, *Appl. Catal. B: Environ.* 153 (2014) 425–436.
- [37] X.J. Guan, L.J. Guo, *ACS Catal.* 4 (2014) 3020–3026.
- [38] B.J. Zheng, X. Wang, C. Liu, K. Tan, Z.X. Xie, L.S. Zheng, *J. Mater. Chem. A* 1 (2013) 12635–12640.
- [39] D.J. Martin, N. Umezawa, X.W. Chen, J.H. Ye, J.W. Tang, *Energy Environ. Sci.* 6 (2013) 3380–3386.
- [40] T. Warang, N. Patel, R. Fernandes, N. Bazzanella, A. Miotello, *Appl. Catal. B: Environ.* 132 (2013) 204–211.
- [41] J. Wan, E.Z. Liu, J. Fan, X.Y. Hu, L. Sun, C.N. Tang, Y.C. Yin, H. Li, Y. Hu, *Ceram. Int.* 41 (2015) 6933–6940.
- [42] M. Salavati-Niasari, A. Khansaric, F. Davara, *Inorg. Chim. Acta* 362 (2009) 4937–4942.
- [43] H. Katsumata, T. Sakai, T. Suzuki, S. Kaneco, *Ind. Eng. Chem. Res.* 53 (2014) 8018–8025.
- [44] G.L. Chen, X.L. Si, J.S. Yu, H.Y. Bai, X.H. Zhang, *Appl. Surf. Sci.* 330 (2015) 191–199.
- [45] G.L. Chen, C. Guyon, Z.X. Zhang, S. Ognier, J. Beem, M. Tatoulian, *Mater. Lett.* 107 (2013) 111–114.
- [46] J.J. Guo, S.X. Ouyang, P. Li, Y.J. Zhang, T. Kako, J.H. Ye, *Appl. Catal. B: Environ.* 134 (2013) 286–292.
- [47] H. Katsumata, T. Hayashi, M. Taniguchi, T. Suzuki, S. Kaneco, *Mat. Sci. Semicon. Proc.* 25 (2014) 68–75.
- [48] Y.F. Wang, X.L. Li, Y.W. Wang, C.M. Fan, *J. Solid State Chem.* 202 (2013) 51–56.
- [49] Y.F. Wang, J.X. Liu, Y.W. Wang, C.M. Fan, G.Y. Ding, *Mat. Sci. Semicon. Proc.* 25 (2014) 330–336.
- [50] S.W. Oh, H.J. Bang, Y.C. Bae, Y.K. Sun, *J. Power Sources* 173 (2007) 502–509.
- [51] H.Y. Hu, Z.B. Jiao, T. Wang, J.H. Ye, G.X. Lu, Y.P. Bi, *J. Mater. Chem. A* 1 (2013) 10612–10616.
- [52] Y.P. Bi, S.X. Ouyang, J.Y. Cao, J.H. Ye, *Phys. Chem. Chem. Phys.* 13 (2011) 10071–10075.
- [53] L.H. Su, Y.G. Wang, S.R. Qiao, J.Q. Zhang, X. Zheng, L.J. Guo, L.H. Sun, Y.J. Sun, Y.L. An, Q. Cao, *Micro Nano Lett.* 4 (2009) 48–52.
- [54] S.W. Zhang, J.X. Li, X.K. Wang, Y.S. Huang, M.Y. Zeng, J.Z. Xu, *ACS Appl. Mater. Inter.* 6 (2014) 22116–22125.
- [55] M. Ge, N. Zhu, Y.P. Zhao, J. Li, L. Liu, *Ind. Eng. Chem. Res.* 51 (2012) 5167–5173.
- [56] T.J. Yan, H.W. Zhang, Y.P. Liu, W.F. Guan, J.L. Long, W.J. Lia, J.M. You, *RSC Adv.* 4 (2014) 37220–37230.
- [57] G. Botelho, J.C. Sczancoski, J. Andres, L. Gracia, E. Longo, *J. Phys. Chem. C* 119 (2015) 6293–6306.
- [58] W.Z. Wang, J. Wang, Z.Z. Wang, X.Z. Wei, L. Liu, Q.S. Ren, W.L. Gao, Y.J. Liang, H.L. Shi, *Dalton Trans.* 43 (2014) 6735–6743.
- [59] Y.P. Liu, L. Fang, H.D. Lu, L.J. Liu, H. Wang, C.Z. Hub, *Catal. Commun.* 17 (2012) 200–204.